Journal of Quantitative Spectroscopy & Radiative Transfer 329 (2024) 109202

Contents lists available at ScienceDirect

Journal of Quantitative Spectroscopy and Radiative Transfer

journal homepage: www.elsevier.com/locate/jqsrt

Experimental determination of the optical properties of walnut shell particles

Matthias Koch [a,*], Stefan Pielsticker [a], Jochen Ströhle [b], Reinhold Kneer [a]

[a] Institute of Heat and Mass Transfer (WSA), RWTH Aachen University, Aachen, Germany
[b] Energy Systems and Technology, Technische Universität Darmstadt, Darmstadt, Germany

ARTICLE INFO

Dataset link: https://doi.org/10.18154/RWTH-2024-08918

Keywords:
Mie theory
Index of refraction
Biomass
Particle radiation interaction
Scattering experiment

ABSTRACT

The index of refraction (IOR) is required to model thermal radiation interaction with pulverized solid fuels. In this work, the complex index of refraction of biomass (walnut shell) is therefore determined using pulverized particles. Single particles are irradiated, and the scattered radiation is measured in different directions. To avoid falsification of the scattering pattern (phase function), the particles are kept contactless in an acoustic levitator. Here, over 1000 different phase functions are measured. The measured scattering patterns are evaluated using an inverse evaluation procedure to determine the IOR. Mie theory serves as the basis for the mathematical modeling of the radiation properties of the particles. The measured IOR is then compared to data from the literature on coal. For the wavelength range $\lambda = 2000$–4000 nm no distinct differences are noticed between the coal and biomass IOR. For $\lambda > 4000$ nm the real part of the biomass IOR is larger and the differences increase with increasing wavelength. However, the order of magnitude still matches that of coal IOR, and thus, only minor differences in the radiative properties of coal and biomass are expected.

1. Introduction

Climate change is one of the biggest challenges facing humanity and is mainly influenced by greenhouse gases (*e.g.*, CO_2) in the atmosphere. One of the largest sources of anthropogenic CO_2 emissions are coal-fired power plants. Since the energy demand is increasing, a sudden shut down of these plants is mostly not possible, and CO_2-neutral methods for these facilities are needed. Possible alternatives include carbon capture and storage (CCS) technologies [1], replacing coal with biomass, or a combination of both technologies. However, designing and developing these technologies, and finally, transferring them to industrial-sized power plants require predictive simulations. Developing such a simulation tool is the goal of a larger collaborative research center, which includes the authors [2]. A part of this research is establishing the fundamentals of the oxy-fuel process for coal and biomass. Hereby the oxy-fuel process describes the combustion in a mixture of recycled flue gas enriched with oxygen instead of air, which enables high CO_2 concentrations, and thus, the sequestration of CO_2 in large combustion facilities [3].

Due to high temperatures and large dimensions in these facilities, radiation is the most dominant heat transfer mechanism [4]. In most cases, particle radiation dominates gas radiation [5]. Particularly in the vicinity of the burner, particle radiation is the decisive heat transfer mechanism. Thus, for an adequate simulation of the combustion process in an industrial combustion chamber, the precise modeling of particle radiation interaction is necessary.

Most models use the Mie theory as benchmark (*e.g.* [6–8]), which gives an analytical solution of Maxwell's equations for radiation interaction with a homogeneous, spherical particle [9]. It provides absorption and scattering efficiency and the scattering phase function. While absorption and scattering efficiency are a measure of the absorbed and scattered quantity, the scattering phase function describes how the scattered radiation is distributed in individual directions [10]. In addition to the size parameter x, which describes the ratio of the particle perimeter $\pi \cdot D_P$ and the wavelength of the interacting radiation λ, the complex index of refraction m (reflectivity and absorptivity properties of the material) is required for the calculation. In order to apply Mie theory, a particle must be spherical and homogeneous. For coal particles with an aspect ratio of less than 1.5, Gronarz et al. [11] showed that Mie theory provides sufficiently accurate approximations for the mentioned radiation properties. A further study showed that it is sufficiently accurate to describe the coal particle by a homogeneous composition [12]. However, most biomasses deviate significantly more from a spherical shape. Koch et al. [13] investigated the radiation properties of artificially generated beechwood particles with porous internal structures and asphericities of 2–6. While the internal structures (*e.g.*, pores) can be approximated by a homogeneous material distribution and thus, an effective refractive index, the aspheric shape cannot be neglected.

To enable the application of Mie theory, this study examines pulverized walnut shells, which have a shape similar to coal particles.

* Corresponding author.
E-mail address: koch@wsa.rwth-aachen.de (M. Koch).

https://doi.org/10.1016/j.jqsrt.2024.109202
Received 24 June 2024; Received in revised form 21 September 2024; Accepted 23 September 2024
Available online 1 October 2024

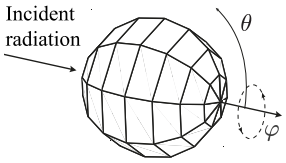

Fig. 1. Illustration of azimuthal angle θ and the polar angle φ.

Differences in radiation behavior can thus be directly attributed to the material properties and are not superimposed by the effects of different particle shapes.

Indeed, there exist data on the complex index of refraction for aerosols of burned biomasses [14], however, the index of refraction for walnut shells or other pulverized biomasses is absent. Literature data on coal also are scarce and show are different to each other. Foster & Howarth [15] observed that the refractive index increases with increasing carbon content in the visible, ultraviolet, and infrared ranges. Mengüç et al. [16] experimentally investigated the scattering of thermal radiation by coal particles and determined a wavelength-independent IOR. Brewster and Kunitomo [17] determined the IOR using an extinction method. However, the accuracy of this approach was questioned by others in later publications [18]. Spectrally resolved data of the IOR of coal were obtained by Manickavasagam and Mengüç [19] using an FTIR measurement. Koch et al. [20] determined the IOR of coal for cold and reacting particles in the visible and near-infrared regions. Both publications analyzed and evaluated the scattering pattern of a single particle to calculate the IOR.

This study uses a similar experimental setup as in [20] to measure the scattering phase function of pulverized walnut shell particles. Here, the detector was replaced to measure the index of refraction for the infrared region. The measured scattering phase function serves as input for the inverse calculation model, which determines the index of refraction. For this purpose, the phase function is calculated using Mie theory and an initial value for the index of refraction. The index of refraction is then varied in a least square method to minimize the difference between the experimental data and the calculated phase function. In the final step, the index of refraction determined for the walnut shell is compared to literature data for coal.

2. Methods

In this section, basic physical phenomena are introduced that occur when a single particle is irradiated. Particular attention is paid to the scattering of radiation by a single particle. Subsequently, simplifications and a suitable modeling approach are presented.

2.1. Radiation scattering

When an electromagnetic wave propagates in a vacuum, its intensity and direction of propagation are constant. However, when the electromagnetic wave interacts with an obstacle, the electric charges within the obstacle are excited and set into oscillatory motion. Due to this motion, electromagnetic energy is radiated in all directions. This phenomenon is called radiation scattering [21]. Despite the reradiation, part of the incident electromagnetic energy is transformed into thermal energy. This phenomenon is called radiation absorption.

Here, it is assumed that the wavelength λ of the scattered wave equals the wavelength of the incident wave, neglecting inelastic scattering. Additionally, this study considers only cases in which a planar electromagnetic wave with constant energy distribution entirely irradiates the obstacle.

To quantify the scattered wave, the intensity I, the azimuthal angle θ and the polar angle φ are introduced. The intensity I is defined as the energy flux per unit area of the scattered wave, and scattering angles give the direction of the scattered wave, where θ ranges from 0–180° and φ ranges from 0–360°. Therefore, $\theta = 0°$ is the forward direction and $\theta = 180°$ the backward direction. These angles are also illustrated in Fig. 1.

The scattered intensity I is also defined by the following equation [22]:

$$I = \frac{I_0 \cdot F(\theta, \varphi)}{k^2 r^2} \tag{1}$$

I_0 is the intensity of the incident electromagnetic wave, r a distance, and k the wave number with $k = 2\pi/\lambda$. F is a dimensionless function that depends on the orientation of the obstacle and the scattering angles, and thus, it is independent on the distance between any point and the particle. This dimensionless function F, also called scattering function, is interpreted as a redistribution function which gives the proportion of scattered intensity I of the original intensity I_0. Dividing F by $k^2 \cdot C_{\mathrm{Sca}}$ finally leads to the phase function Φ which has a more practical use. Physically, C_{Sca} describes the area on which the incident electromagnetic wave is influenced due to scattering, and thus, it is also calculated by integrating F over all directions applying the following equation:

$$C_{\mathrm{Sca}} = \frac{1}{k^2} \int F(\theta, \varphi) \cdot \sin(\theta)\, d\theta d\varphi \tag{2}$$

Due to diffraction, the scattering cross section C_{Sca} is larger than the geometrical cross section G of the obstacle. Similar to the scattering cross section, also an absorption cross section C_{Abs} exists, which can also be larger than one [23]. In order to compare the absorption/scattering cross section of different bodies, the absorption/scattering efficiencies Q are used which resemble the ratio of radiation cross section to geometrical cross section.

All in all, phase function Φ, scattering and absorption cross section C represent the radiative properties of an obstacle interacting with an electromagnetic wave. While the cross sections are quantities to determine *how much* radiation is scattered and/or absorbed, the phase function determines *in which direction* the radiation is scattered. In this study, the interacting obstacle is a pulverized walnut shell particle, and thus, the calculation and the simplifications of the radiative properties for particles are discussed in the following section.

2.2. Modeling particle radiation interaction

To determine the radiative properties of a single particle interacting with electromagnetic waves, Maxwell's equations are solved. Usually, numerical exact methods like the discrete dipole approximation (DDA) [24] are used. Thereby, the particle is divided into small regions, and dipoles replace these regions. The incident electromagnetic wave induces a dipole moment in each region, and due to the oscillation of the dipoles, radiation is scattered in different directions. Therefore, this method mimics the microscopic behavior of the electric charges within the particle. With decreasing size of these dipole regions, the discrete dipole approximation is an exact method.

The advantage of the method is that there are no restrictions on its application. Any shape as well as internal inhomogeneities can be modeled. However, the drawback of this method is cause by its computational costs. Aside from the drastically increased calculation time, this method needs a non-realizable amount of memory for particles that are large compared to the incident wavelength. Due to the sizes of the particles investigated, this method is not realizable. For the application of other methods, the shape of the particle and the composition needs to be simplified. For homogeneous and axisymmetric particles, the semi-analytical T-Matrix method [25] can be applied. Similar to the DDA, the computational costs are not realizable for particles which are large compared to the wavelength. Then, different theories exist to determine phase function and cross section for homogeneous spheres depending

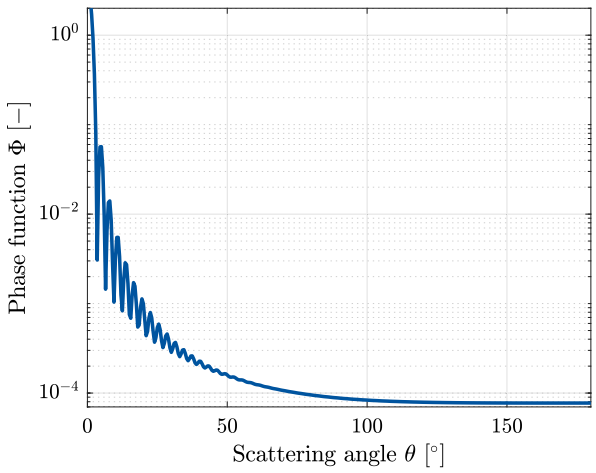

Fig. 2. Phase function for $x = 60$ and $m = 1.8 + 0.2\mathrm{i}$ [16].

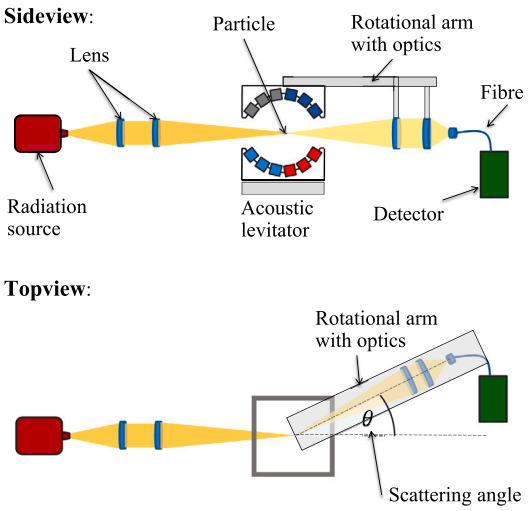

Fig. 3. Schematic illustration of the experimental setup.

on the sphere's size. To distinguish between the application of these theories, the size parameter x

$$x = \frac{\pi \cdot D_\mathrm{P}}{\lambda} \tag{3}$$

is introduced with D_P denoting the particle diameter and λ the wavelength. The following regimes exist:

- $x \ll 1$ — Rayleigh-scattering [26]
- $x \approx 1$ — Mie-scattering [9]
- $x \gg 1$ — Geometrical optics [27]

The Mie theory [9] is an analytical solution of Maxwell's equation for a homogeneous sphere, and thus, applicable for all size parameters. The solution by Rayleigh [26] for $x \ll 1$ and the geometrical optics solution for $x \gg 1$ represent approximations of Mie theory with less computational costs and a negligible error. In this study, the Mie theory is applied for the evaluation of the scattering experiment. Therefore, the particle is assumed to be spherical and homogeneous. A detailed description of Mie theory is given by Bohren & Huffman [21], and the following calculations are based on the implementations by Mätzler [28]. The Mie theory requires as input the size parameter, and the complex index of refraction m (IOR) of the particle,

$$m = n + k\mathrm{i} \tag{4}$$

The real part n is the ratio of the speed of light in vacuum to the speed of light in the material and the imaginary part k takes into account the absorption strength of the material. Fig. 2 illustrates exemplarily a Mie phase function for $x = 60$ and $m = 1.8{+}0.2\mathrm{i}$ depending on scattering angle θ. The IOR corresponds to the measured IOR for coal particles by Mengüç et al. [16]. As mentioned in Section 2.1 $\theta = 0°$ means forward and $\theta = 180°$ means backward scattering. Due to the rotational symmetry of a sphere, θ is sufficient to describe the phase function in all directions. Most of the radiation is scattered in forward direction and with increasing scattering angle θ the value of the phase function decreases, and thus, the scattered radiation. For $0° < \theta < 50°$ oscillations are noticeable. These scattering lobes originate from the superposition of the diffracted and scattered waves. With smaller size parameters, these scattering lobes are also clearly visible at larger scattering angles. With increasing size parameters, the scattering lobes are limited to a decreasing angle range near $\theta = 0°$.

3. Experimental setup & evaluation method

For the acquisition of scattered radiation, the setup displayed in Fig. 3 was used. The setup is basically the same as in Koch et al. [20], but the levitator has been upgraded and the detector replaced. The radiation emitted by the source is focused by lenses on the particle, which is kept in position by an acoustic levitator, and the scattered radiation is collected by lenses connected via a fiber to a detector. Afterwards, the particle is taken out from the levitator and the equivalent particle diameter is determined.

In the following sections the components of the experimental setup are briefly introduced. Since, the radiation is collected by a circular lens, the phase function has to be integrated over this circular area. Therefore, the assessment to build a phase function from the scattering signals is explained and afterwards, the inverse evaluation method to determine the complex index of refraction is presented.

3.1. Radiation source

The IOR is wavelength-dependent, and thus, a broadband radiation source is required. In this study, a silicon carbide light source is used. The housing of the silicon carbide is provided by THORLABS (SLS203L) and consists of an ellipsoid reflector and a CaF_2 collimating lens with a focal length of 40 mm. The outgoing radiation is almost collimated and ranges from 0.5–9 µm. Furthermore, its intensity distribution is comparable to that of a blackbody radiating at a temperature of 1500 K, where the peak of the radiation intensity distribution is shifted to 2400 nm. The intensity distribution normalized by its maximum is illustrated in Fig. 4 by the black curve. This radiation is focused by a second CaF_2 lens with a focal length of 75 mm onto the levitated particle. Here, the beam waist diameter in the focal plane extends to a few millimeters. As the particle is smaller than one millimeter, it is assumed that the entire particle is irradiated by a constant radiation field.

3.2. Acoustic levitator

In the experiment, it is essential to apply a non-intrusive method to keep the particle in position. Otherwise, any holding feature which interacts physically with the particle could falsifies the scattering pattern. Therefore, an acoustic levitator was set up to keep the particle in position without physical contact. Here, the necessary acoustic field is created by the superposition of sound waves emitted by a number individual sound sources. The basic principle is explained by Marzo et al. [29,30]. The levitator consists of 2 shells, each with four speaker rings equipped with 4, 8, 16, and 16 sources from the inside to the outside. In total, the levitator consists of 88 sound sources, all aligned to the center. The emitted sound waves are superimposed in the levitator, creating an interference pattern. The generated force counteracts the

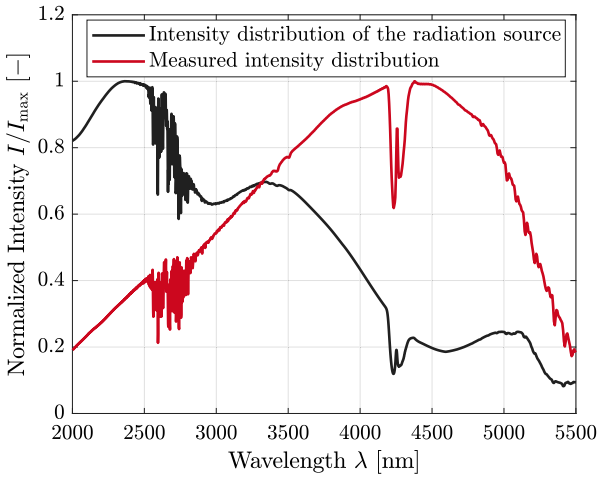

Fig. 4. Real intensity distribution (black) and measured intensity distribution (red) — The difference originates from the detector's sensitivity.

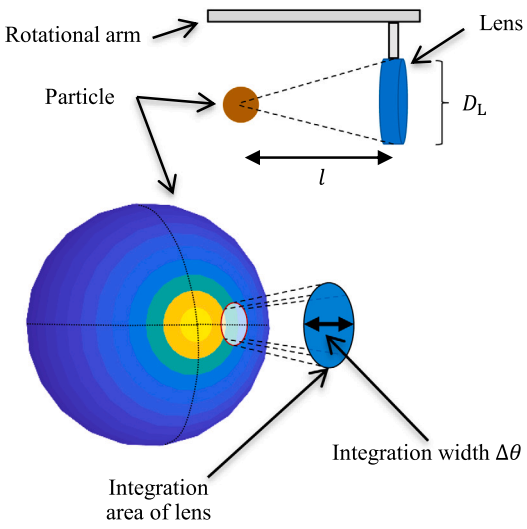

Fig. 5. Phase function plotted on a sphere — Since the scattered radiation is collected by a circular lens, the phase function is integrated over the shown circular area.

gravitational force, while additional lateral forces keep the particle in position.

In comparison to Koch et al. [20] the number of sound sources is increased by adding an additional ring of sound sources to increase especially the lateral forces. Since all sound sources point to the center, the best levitation point is at the center. When the particle is set close to the center, it is accelerated towards the center by the sound pressure. For the placement, a fine, soundwave-permeable mesh is used. Due to their imperfect shape, levitated particles typically rotate around the z-axis. It is possible to levitate walnut shells with an equivalent diameter of 150–2000 µm. With decreasing diameter, the relative fraction of scattered radiation increases compared to larger particles. However, the absolute fraction of scattered radiation decreases due to the smaller surface area. Therefore, pulverized walnut shell particles from a sieving of 450–600 µm are used in the experiment.

3.3. Radiation acquisition and detection

The scattered radiation is collected by lens optics, which are mounted to a rotational arm. The center of the rotational axis coincides with the z-axis and thus, with the position of the particle. The lens optics consists of two CaF_2 lenses, each with a focal distance l of 40 mm and a diameter D_L of 25.4 mm. The first lens is positioned at a distance of 40 mm to the particle. It collects and collimates the scattered radiation. The second lens is placed behind the first one and focuses the collected radiation onto the input of an indium fluoride glass fiber with a core diameter of 200 µm.

The angle of the rotational arm can be set to $\theta = 0$–$114°$. For $\theta > 114°$, the rotational arm would block the path between the radiation source and the particle. Therefore, only angular positions up to $\theta = 114°$ were considered. However, the scattered radiation was only measured every three degrees for the range of $\theta = 21$–$114°$, resulting in $N_{angle} = 32$. For $\theta < 21°$, the fraction of emitted radiation that radiates directly from the source into the lens optic disturbs the measurement.

For the evaluation of the scattered radiation, an FTIR spectrometer is used (ARCoptix FT-MIR 'Rocket' spectrometer). The spectrometer supports wavelengths ranging from $\lambda = 2000$–6000 nm and thus, it covers the most important range of the radiation in a combustion chamber. Fig. 4 displays the measured radiation signal divided by its maximum (red), when the broadband source directly radiates into the spectrometer (no scattering). The black curve indicates the real intensity distribution of the radiation source divided by its maximum. From the difference between these two curves, it is concluded, that the sensitivity of the spectrometer for $\lambda = 2000$–4500 nm is lower than for the remaining part, especially for the range $\lambda = 2000$–3000 nm.

For the assessment of the phase function utilizing the measured scattering data, the phase function is integrated over the circular area of the lens,

$$\Phi_{\Delta\theta,i} = 2 \cdot \int_{\theta^* - \frac{\theta}{2}}^{\theta^* + \frac{\theta}{2}} \Phi(m, x, \theta) \cdot \sin(\theta) \cdot \sin(\varphi^*)\, d\theta \tag{5}$$

The integration width results from the diameter of the collecting lens D_L and its focal length l,

$$\Delta\theta = \arctan\frac{D_L}{l} \tag{6}$$

To consider the 3-dimensional nature of the phase function, the integral is multiplied by $\sin(\theta)$. The angle φ^* is introduced to resemble the integration over the circular collector.

The relation between integration area, integration width and the scattering phase function is illustrated in Fig. 5. The scattering particle is represented by a colored sphere. The color code indicates the value of the phase function plotted on the surface of the sphere. The integration area on the sphere is marked by a red circle.

For the acquisition of the raw data, 5 measurements are averaged and saved over a time of roughly 500 ms. This internal averaging process is repeated 50 times at each angle. Fig. 6 displays exemplarily the raw data for a scattering angle $\theta = 33°$. To minimize the influence of noise, a low-pass filter is applied to the raw data using the seven low-frequency modes of the fast Fourier spectrum. The filtered signal is shown by the dashed curve.

Although the spectrometer evaluates radiation ranging from 2000–6000 nm, the scattered signal is evaluated only for 2000–5500 nm. The scattered signal is steadily decreasing for a wavelength $\lambda > 5500$ nm and thus, too noisy. Furthermore, due to the amount of data, the phase function is discretized with a step size of 50 nm and a starting point at 2050 nm.

3.4. Equivalent diameter determination

Each particle is collected after the scattering signal is recorded completely. Then, the particle is photographed from various positions under a microscope. Fig. 7 shows an example of a pulverized walnut shell particle. The particle is assumed to have a cylindrical shape, and the resulting volume-equivalent diameter of a sphere is determined

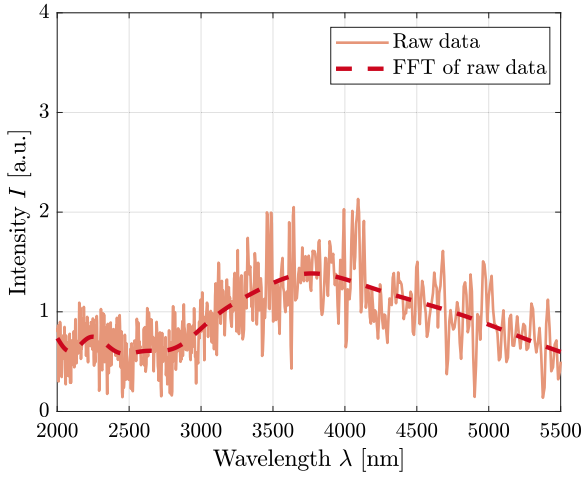

Fig. 6. Measured rawdata and filtered signal for scattering angle $\theta = 33°$.

Table 1
Equivalent particle diameter and axis ratios of the WNS.

	D_P [µm]	Axis ratio [−]		D_P [µm]	Axis ratio [−]
# 1	568.1	1.27	# 2	514.7	1.45
# 3	613.5	1.28	# 4	556.8	1.30
# 5	543.3	1.30	# 6	567.1	1.33
# 7	647.1	1.16	# 8	667.7	1.41
# 9	681.5	1.16	# 10	729.9	1.26
# 11	603.7	1.24	# 12	593.7	1.24
# 13	856.7	1.38	# 14	827.3	1.11
# 15	671	1.18			

graphically with the help of such an image. For the illustrated particle, the resulting equivalent diameter is $D_P = 613.5\,\mu m$ with an axis ratio of 1.28.

The equivalent diameters D_P and the axis ratios of the remaining walnut shell particles (WNS) are listed in Table 1.

3.5. Inverse problem

An inverse problem generally describes calculating the cause of a unique effect [31]. In the context of this study, the inverse problem is the determination of the IOR (the cause) for the measured phase function (the effect of radiation interacting with a particle). To solve this inverse problem, the direct problem needs to be defined, which is the calculation of a discrete phase function. The wavelength of the incident radiation λ, the particle diameter D_P, the integration limits $\Delta\theta$ and angles θ as well as the IOR m are *input variables*. Then, the direct problem is divided into two steps: (1) Applying wavelength, particle diameter, and IOR to Mie theory results in a continuous phase function Φ, and (2) this continuous phase function is integrated applying Eq. (5) with the defined integration limits and angles. The integration yields the *output variable* of the given direct problem — the integrated phase function $\Phi_{\Delta\theta}$.

In the inverse problem, some input variables (D_P, λ, $\Delta\theta$ and θ) and the output variable ($\Phi_{\Delta\theta}$) are known. To determine the remaining input variable (IOR m), the inverse problem is transferred into an optimization problem with a functional that has to be minimized. In this study, the optimization problem is stated as

$$\text{minimize}_{m\in\mathbb{C}}\,\Delta\Phi(m), \tag{7}$$

where the following definition for the functional $\Delta\Phi(m)$ is implemented:

$$\Delta\Phi = \sum_{i=1}^{N_{\text{angle}}} \frac{\text{abs}\left(\log(\Phi_{\Delta\theta_i,\text{meas}}) - \log(\Phi_{\Delta\theta_i,\text{calc}})\right)}{\text{abs}\left(\log(\Phi_{\Delta\theta_i,\text{calc}})\right)} \tag{8}$$

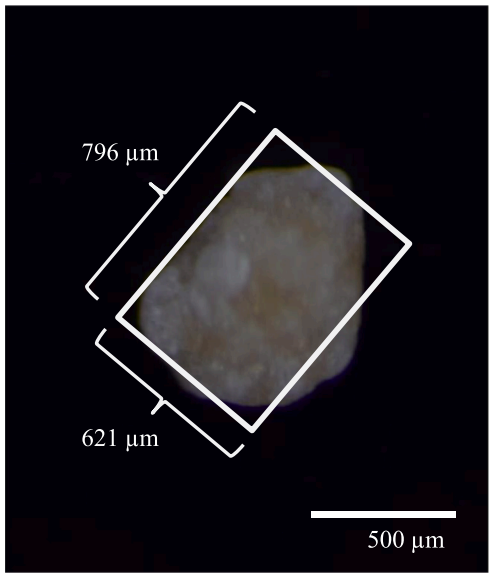

Fig. 7. Pulverized walnut shell particle — The volume-equivalent diameter of a sphere is calculated by approximating the shape of the particle by a cylinder.

The indices *meas* and *calc* are short for *measured* and *calculated*, thus, $\Phi_{\Delta\theta_i,\text{meas}}$ and $\Phi_{\Delta\theta_i,\text{calc}}$ represent the measured and calculated integrated phase function in the ith angle. The total number of investigated angles is defined by $N_{\text{angle}} = 32$. All in all, this function represents the difference between calculated and measured values, summed over each integration interval.

For the calculation of $\Phi_{\Delta\theta_i,\text{calc}}$ a random start value for $m_0 = n_0 + k_0\text{i}$ is set. Subsequently, the summed difference $\Delta\Phi$ is minimized by changing the IOR applying the interior point method [32] implemented in the Matlab routine fmincon. Here, n is constrained to be larger than 1, and k to be larger than 0. The first constraint ensures that the particle is optically thicker than the vacuum, and the second constraint is a physical constraint since the absorptivity index k is not defined for values smaller than 0. During this routine, the particle radiation interaction is evaluated for different combinations of n and k. Due to this multiple repetition of the direct problem, methods like the discrete dipole approximation or the T-Matrix method are technically not feasible considering the calculation time of solving a single direct problem.

In the study by Koch et al. [20] this routine was validated and applied to determine the IOR of Colombian bituminous coal for $400\,\text{nm} \leq \lambda \leq 950\,\text{nm}$.

4. Results and discussion

In this section, first, the phase function of a single particle is exemplarily illustrated and described. As the scattering patterns of various particles are recorded and evaluated, the characteristics of all phase functions are finally summarized and the IOR is presented. In the last step, the measured IOR of the WNS is compared to the measured IOR of coal particles in various literature studies.

4.1. Scattered intensities & the corresponding phase functions

Fig. 8 depicts examples of the measured scattered intensity I_{Sca} for three different wavelengths, and the sum of the scattered intensity over each angle. Therefore, Figs. 8(a) and 8(b) display the measured absolute values of scattered radiation. Due to the lower sensitivity of the detector for $\lambda < 3500\,\text{nm}$, the measured intensity for this wavelength range is lower, especially for the wavelengths $2500\,\text{nm} < \lambda < 3000\,\text{nm}$.

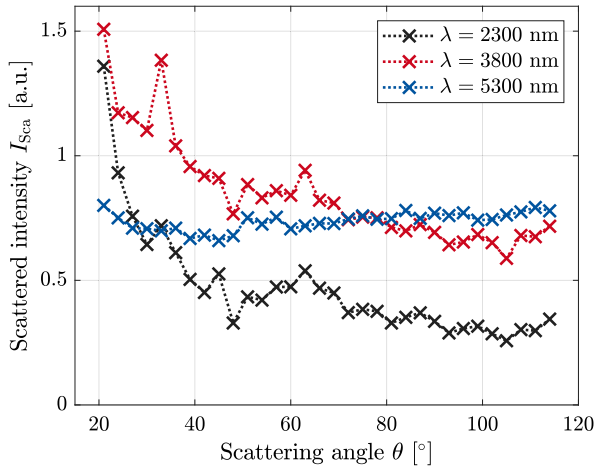

(a) Scattered intensity $I_{Sca,\lambda}$

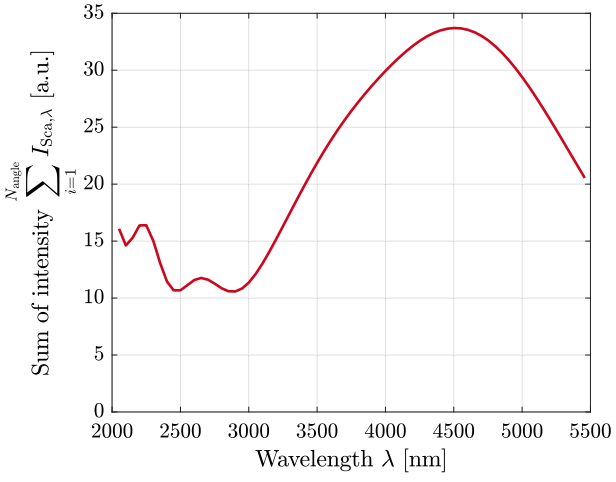

(b) Sum of scattered intensity $\sum_{i=1}^{N_{angle}} I_{Sca,\lambda}$ of a single particle

Fig. 8. (a) Measured scattered intensity I_{Sca} for three wavelengths (b) The sum of scattered intensity depending on the wavelength.

The phase function depends on the scattered intensity I_{Sca} and its sum, and thus, it is interpreted as the relative amount of the scattered intensity. For its calculation utilizing the shown intensities, the following equation is applied,

$$\Phi_\lambda(\theta_i) = I_{Sca,\lambda}(\theta_i) \cdot \left(\frac{1}{4\pi} \sum_{i=1}^{N_{angle}} I_{Sca,\lambda}(\theta_i) \right)^{-1}, \tag{9}$$

and the resulting phase functions are illustrated in Fig. 9. Analyzing just the phase function displayed in Fig. 9, the following characteristics are noticed. The largest value of the phase function is measured at $\theta = 21°$ for all three wavelengths. Furthermore, with increasing wavelength, the peak of Φ at $\theta = 21°$ decreases, while the values of the phase function for $\theta > 60°$ increase. However, the smallest value of the phase functions is not necessary at $\theta = 114°$, especially for $\lambda = 5300\,\text{nm}$. The phase functions with $\lambda < 5300\,\text{nm}$ indicate an almost steady decrease with increasing scattering angle up to $\theta = 105°$. Afterwards, the values of Φ increase to the same value of Φ at $\theta = 72°$. The phase function for $\lambda = 5300\,\text{nm}$ seems to reach its lowest value already at a scattering angle around $\theta = 45°$.

However, considering the absolute amount of scattered radiation, the phase functions for $\lambda < 3500\,\text{nm}$ are more prone to measurement

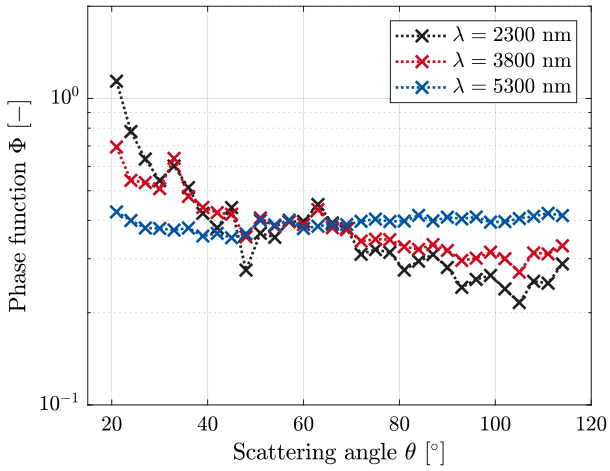

Fig. 9. Three examples of the measured phase functions utilizing the filtered signals. The phase functions are measured using particle 14.

noise and thus, are less accurate. A small measurement error for the value at $\theta = 21°$ has more impact on the phase function for this wavelength range than a small error for the remaining wavelengths.

For a general interpretation of all measured phase functions, Fig. 10 displays the probability of an angle having the highest, second highest, third highest, etc., value of all measured phase functions. Since the scattered radiation is evaluated in 32 angles, Fig. 10 shows 32 columns with 32 different color codes. Black to red represents a low probability, and yellow to white a high probability. The first column shows the probability distribution for the first angle (21°). In other words, the top value indicates the likelihood of the first angle having the highest value, the color coding below indicates the likelihood that the first angle has the second highest value, and so on. The second column describes the same distribution only about the second angle (24°), and the other columns follow this pattern. If a strictly monotonically decreasing function could describe each phase function, then each entry would be shown in black, and only the diagonal would be shown in white. This is not the case for the measured phase functions, however, higher probability color codings are close to the diagonal. The following statements are concluded:

- In 70 % of the cases, the phase function Φ has its largest value at $\theta = 21°$
- The mean value of the diagonal is 13 % (excluding the entry for $\theta = 21°$)
- With 22 %, $\theta = 105°$ has the highest probability to be the angle with the lowest value for the phase function Φ
- The last angle $\theta = 114°$ has a probability of 14 % to be the angle with the lowest value for the phase function Φ
- It is better to approximate the measured phase functions curvature by a convex function than by a concave function
- For $\lambda < 2500\,\text{nm}$ the variance of the phase functions value increases, while for $\lambda > 2500\,\text{nm}$ the variance decreases. This also means, for $\lambda < 2500\,\text{nm}$ the peak value at $\theta = 21°$ increases, and for $\lambda > 2500\,\text{nm}$ with increasing wavelength the peak value at $\theta = 21°$ decreases.

4.2. Determination of the WNS ior

The procedure described in Section 3.5 is applied to determine the complex index of refraction. This procedure results in a best-fitting calculated phase function and the corresponding IOR of this calculated phase function. Fig. 11 illustrates the measured phase function and the resulting calculated phase functions exemplarily for three wavelengths

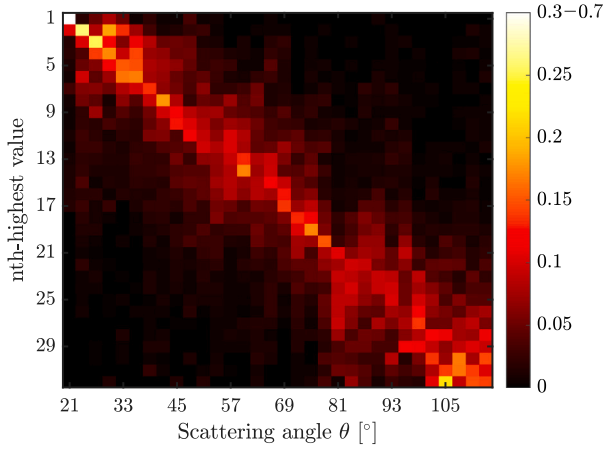

Fig. 10. Probability distribution of angle distribution. The colorbar on the right side indicates the value of the probability. White means that 100 % of all phase functions have the nth highest value and black means 0 %.

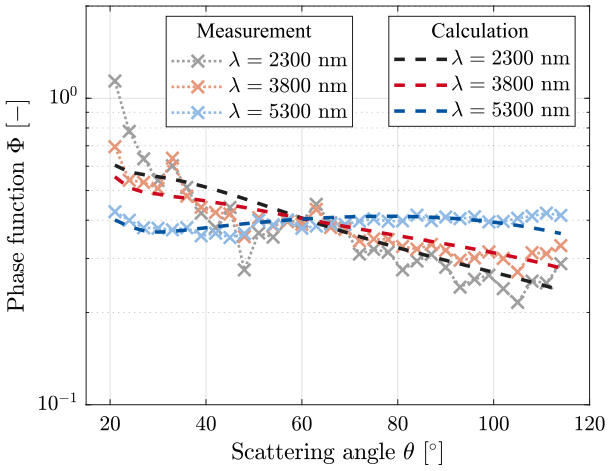

Fig. 11. 3 Examples of the best fit phase functions compared to the measured phase function: Crosses mark the measured phase functions, which are also displayed in Fig. 9. The dashed lines indicate the calculated phase function.

for one individual particle. The overall trend is approximated, however, the deviation between the measured and calculated phase function for $\lambda = 2300\,\text{nm}$ is more significant than for the other wavelengths. Especially the approximation of the forward angles gets worse with decreasing wavelength. For the goodness-of-fit analysis, the mean deviation of all phase functions depending on the wavelength is calculated applying Eq. (10),

$$E_\lambda = \sum_{i=1}^{N_\text{Particles}} \frac{\Delta\Phi_\text{i}}{N_\text{Particles} \cdot N_\text{angle}} \tag{10}$$

This relation is also illustrated in Fig. 12. The largest deviations are recognized for $2200\,\text{nm} < \lambda < 3450\,\text{nm}$. In this region, the deviation is $15\,\% < E_\lambda < 20\,\%$. Afterwards, the deviation decreases and for $\lambda > 4100\,\text{nm}$ it is smaller than 10 %.

To calculate the deviation angle-dependent, the mean deviation of all phase functions depending on the angle is calculated (not graphically displayed). The largest deviations are noticed (similar to Fig. 11) for the first angle. Here, the average deviation of all wavelengths for $\theta = 21°$ is 37 %. The mean deviation of the remaining angles is around 10 %. Therefore, the course of the deviation E_λ mainly results from the deviation of the first angle between the measured and the calculated phase function. This might result from simplifications of the particle

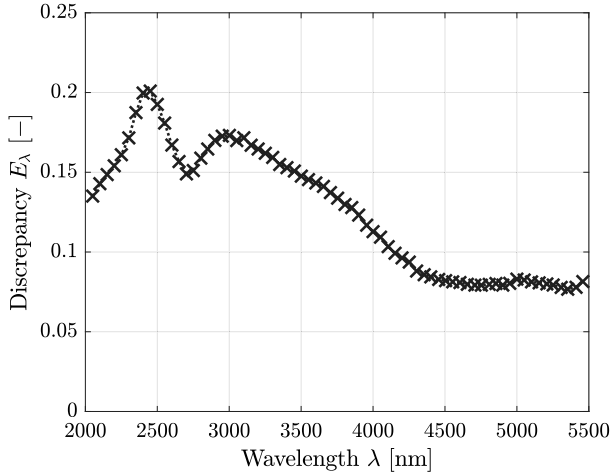

Fig. 12. Mean discrepancy of measured and calculated phase function applying Eq. (10).

shape. In Koch et al. [13], the influence of internal structure as well as the shape of biomass particles was investigated numerically. The results show that particles with increasing axis ratios indicate an increasing fraction of forward scattering. This relation justifies why the deviation of the first angle is the largest. The decreasing trend with increasing wavelength results from the sensitivity of the detector and the absolute values of scattered intensity per wavelength. In the previous section, it is highlighted, that less radiation is measured for $\lambda < 3500\,\text{nm}$, and thus, the measured phase function is more prone to measurement noise. Further detectors for the range $\lambda < 3500\,\text{nm}$ were tested, but the used FTIR spectrometer indicated the best results.

Fig. 13 displays the resulting complex index of refraction. Red indicates the real part n, blue indicates the imaginary part k, where crosses mark the determined values for each particle, and the dashed line specifies the average IOR of all particles. The overall course of the real part and the imaginary part are comparable. For $2000\,\text{nm} < \lambda < 2500\,\text{nm}$ the value of real and imaginary part decreases, and for $\lambda > 2500\,\text{nm}$ these values increase.

Then, the mean value of n and k are fitted by a second order polynomial. The following polynomials are used for the real part n and the imaginary part k:

$$n(\lambda) = 5.8 \cdot 10^{-8}\text{nm}^{-2} \cdot \lambda^2 - 2.8 \cdot 10^{-4}\text{nm}^{-1} \cdot \lambda + 2.0 \tag{11}$$

$$k(\lambda) = 2.0 \cdot 10^{-8}\text{nm}^{-2} \cdot \lambda^2 - 1.1 \cdot 10^{-4}\text{nm}^{-1} \cdot \lambda + 0.3 \tag{12}$$

Furthermore, the IOR is antiproportional to E_λ. This antiproportionality results from the antiproportionality of the IOR to the value of the forward peak at $\theta = 21°$. When this value increases, the IOR decreases, and when this value increases, the IOR decreases. Since the deviation E_λ mainly depends on the deviation between the measured and calculated forward peak, the same antiproportionality results between IOR to E_λ. This antiproportionality also explains the overall course of the IOR. With increasing wavelength, the measured forward peak decreases. Consequently, the IOR increases.

Despite the functional shown in Eq. (8), the following functionals are also applied to minimize the difference between calculated and measured phase function:

$$\Delta\Phi = \sum_{i=1}^{N_\text{angle}} \frac{\text{abs}\left(\Phi_{\Delta\theta_i,\text{meas}} - \Phi_{\Delta\theta_i,\text{calc}}\right)}{\text{abs}\left(\Phi_{\Delta\theta_i,\text{calc}}\right)} \tag{13}$$

$$\Delta\Phi = \sum_{i=1}^{N_\text{angle}} \text{abs}\left(\Phi_{\Delta\theta_i,\text{meas}} - \Phi_{\Delta\theta_i,\text{calc}}\right) \tag{14}$$

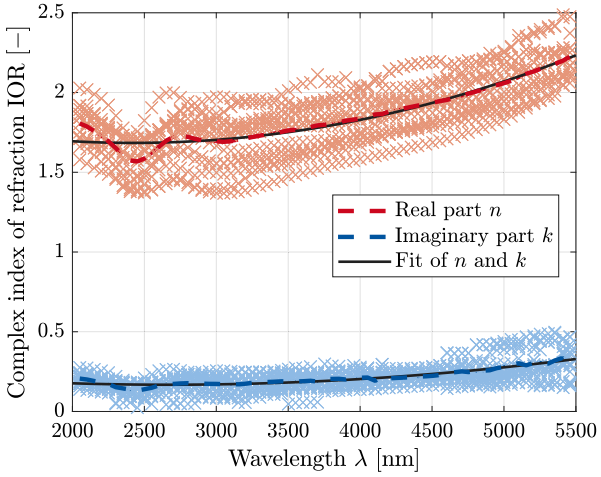

Fig. 13. Real and imaginary part of the determined IOR for WNS depending on the wavelength: The crosses mark the measured values and the dashed line indicates the mean value of all measurements. The black curves illustrate a fit of the mean value by a second order polynomial.

$$\Delta\Phi = \sum_{i=1}^{N_{\text{angle}}} \text{abs}\left(\log(\Phi_{\Delta\theta_i,\text{meas}}) - \log(\Phi_{\Delta\theta_i,\text{calc}})\right) \tag{15}$$

However, no significant difference for the IOR has been noticed.

4.3. Comparison of the index of refraction for WNS and coal

This chapter estimates how replacing coal with biomass affects radiation exchange within a combustion chamber. Since the particle of WNS can be approximated by a sphere due to its low asphericity, the differences in radiation exchange of coal and WNS are directly coupled to the IOR. Therefore, Fig. 14 illustrates different wavelength-dependent indices of refraction of coal from several studies and the fit of the determined WNS IOR. Set 1 was measured by Brewster et al. [17]. They used an extinction method to determine the IOR. Set 2 is based on the measurements by Foster and Howarth [15]. They evaluated reflected radiation applying Fresnel's laws. Here, among others high volatile coals were evaluated. Later, the data provided by Foster and Howarth was fitted by Johansson et al. [5] and is presented in Fig. 14. Set 3 – 6 is based on measurements by Manickavasagam et al. [19]. They evaluated different types of coal, where the difference consists in the fraction of volatiles. They measured the transmitted and scattered radiation in the forward direction, and applied an inverse evaluation method to determine the IOR.

Fig. 14(a) depicts the real part n of the IOR. Sets 3 – 6 have constant values, where sets 3 and 5 coincide with $n = 1.6$, and sets 4 and 6 coincide with $n = 1.8$. Sets 1 and 2 indicate steady increase with increasing wavelength. All in all, the real part of the coal IOR is between 1.6 and 1.9. For $\lambda < 4250\,\text{nm}$ the WNS IOR lies in the same region. However, for $\lambda > 4250\,\text{nm}$ the WNS IOR leaves this region and with increasing wavelength, the difference between IOR of WNS and coal increases. This difference means, that the phase function for $\lambda > 4250\,\text{nm}$ has a smaller forward peak and a little higher value for the scattering angles of $\theta < 60°$.

Fig. 14(b) depicts the imaginary part k of the IOR. As the imaginary part of the IOR describes the absorption properties of the material, a larger imaginary part means higher absorptivity.

The differences between the coal types are more noticeable compared to the real part. Set 1 indicates the lowest value. It starts with $k \approx 0.045$ at $\lambda = 2500\,\text{nm}$ and decreases steadily to $k \approx 0.01$ at $\lambda = 5500\,\text{nm}$. Contrary, set 2 is constant with a value of $k = 0.3$ up to $\lambda = 5000\,\text{nm}$. Afterwards, it increases steadily. For $\lambda < 3000\,\text{nm}$ set 4 – 6 are constant with $k \in [0.07\ 0.15\ 0.21\ 0.35]$, and then, they

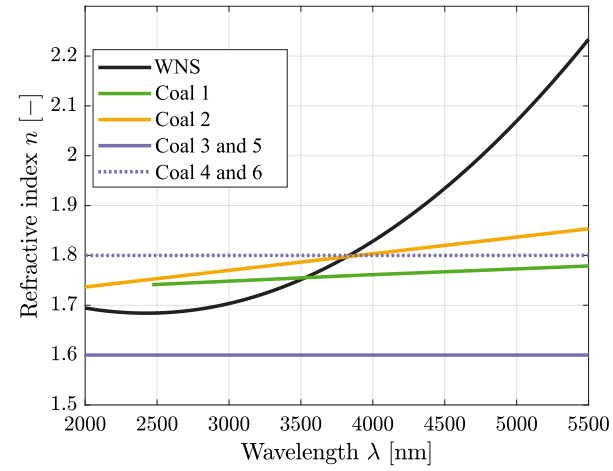

(a) Real part of the IOR

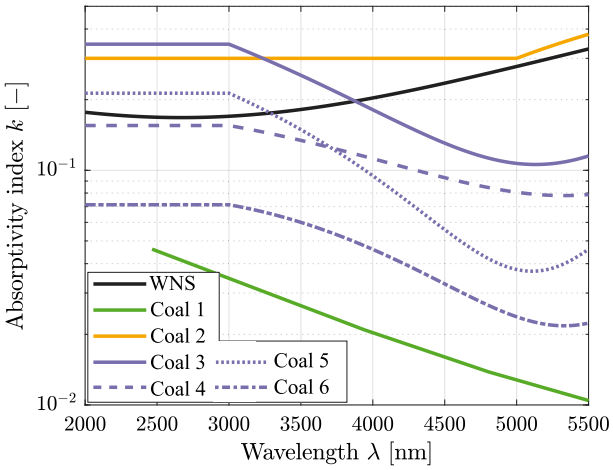

(b) Imaginary part of the IOR

Fig. 14. IOR of coal from various studies and WNS IOR determined in this study — Coal 1 was measured by Brewster et al. [17], Coal 2 was measured by Foster and Howarth [15] and Coal 3–6 was measured by Manickavasagam et al. [19].

decrease with increasing wavelength. The imaginary part of the WNS IOR is also almost constant for $\lambda < 3000\,\text{nm}$ with a value of $k = 0.17$, and thus, comparable to set 4 and 5. Set 2 and 3 indicate ≈ twice the value and set 6 half the value. These differences result in higher and lower absorption properties, but are still comparable. In contrast to set 3–6, the imaginary part increases for $\lambda > 3000\,\text{nm}$ indicating higher absorptivity. However, it does not exceed the value of set 2.

In general, the absorption index is related to the chemical compounds of the material. Due to different functional groups, the absorption properties differ at specific wavelengths. The influence of such functional groups on the absorbance of WNS was investigated by an attenuated total reflection IR-spectroscopy by Böttger et al. [33]. For example, higher water content (O-H stretching) or cellulose/hemicellulose (C-O-C stretching) increase absorptivity at some wavelength ranges compared to the investigated coal. However, there is no detection of a specific functional group that justifies the increased absorption index of WNS for the wavelength range 3000–5000 nm.

All in all, the radiative properties of the WNS coincide roughly with the ones of set 2, which represents a high volatile coal, and the largest deviations are noticed for set 1 due to its much lower imaginary part k. The large difference of set 1 to the remaining measurements originates from the used method of the authors. Brewster et al. used an extinction method to determine the IOR. All other measurements (including this

study) are based on a scattering/reflection methods. The accuracy of the measurements by Brewster et al. was already questioned by [18].

5. Conclusion & summary

In this study, the scattering pattern of 15 pulverized walnut shell particles (WNS) was measured in the wavelength range 2000–5500 nm for scattering angles of $21° \leq \theta \leq 114°$. These measurements were used to construct the phase function and then calculate the complex index of refraction (IOR). Over 1000 phase functions were constructed. Here, an inverse calculation method based on Mie theory was used to determine the IOR. Subsequently, the determined IOR of WNS was compared with data from the literature on coal.

The measured phase functions indicate a decreasing trend with increasing scattering angle. 70 % of all measured phase functions have their peak value at $\theta = 21°$. The peak value decreases with increasing wavelength λ, and the fraction of backward scattering increases. The best-fit calculated phase functions are in good agreement with the measured phase functions: For $\lambda < 3450$ nm the mean relative deviation of measured and calculated phase function is between 15–20 %; for $3450\,\text{nm} < \lambda < 4100\,\text{nm}$ between 10–15 %; for $\lambda > 4100$ nm smaller than 10 %. The mean deviation of the calculated and measured forward peak decreases with increasing wavelength, and the largest mean deviation of the calculated and measured phase function is at $\theta = 21°$.

The determined IOR is wavelength-dependent and was fitted by a second-order polynomial. For $\lambda < 3000$ nm, the polynomials for real and imaginary part of the WNS IOR are constant with $n = 1.69$ and $k = 0.17$, respectively. For $\lambda > 3000$ nm, both polynomials increase to maximum values of $n_{max} = 2.23$ and $k_{max} = 0.33$. The increase in its value results from the decrease of the forward peak.

Finally, the resulting WNS IOR was compared to literature data on the coal IOR. For $\lambda < 4000$ nm, it is in agreement with all compared coals despite the set determined by Brewster et al. [17] due to its low imaginary part. For $\lambda > 4000$ nm, the best coincidence is with the set by Foster and Howarth [15]. Since Foster and Howarth used high volatile coal, WNS possess similar radiative properties as this type of coal. Overall, WNS feature a larger imaginary part than all coals except the coal evaluated by Foster and Howarth. This results in slightly higher absorption and less scattering.

CRediT authorship contribution statement

Matthias Koch: Writing – original draft, Visualization, Validation, Methodology, Investigation, Conceptualization. **Stefan Pielsticker:** Writing – review & editing, Supervision, Conceptualization. **Jochen Ströhle:** Writing – review & editing. **Reinhold Kneer:** Writing – review & editing, Supervision.

Declaration of competing interest

The authors declare that they have no known competing financial interests or personal relationships that could have appeared to influence the work reported in this paper.

Data availability

The datasets presented in this study can be found in: https://doi.org/10.18154/RWTH-2024-08918.

Acknowledgment

This work has been funded by the Deutsche Forschungsgemeinschaft (DFG, German Research Foundation) within the project SFB/TRR 129 “Oxyflame” (No. 215035359).

References

[1] Chen W-Y, Suzuki T, Lackner M. Handbook of climate change mitigation and adaptation. Springer International Publishing Cham, Switzerland; 2017.
[2] Development of methods and models to describe solid fuel reactions within an oxy-fuel atmosphere. 2022, URL https://www.oxyflame.de.
[3] Degtiarev V, Gribovski V. Carbon dioxide semi-closed power plant. Bull Inventions 1967.
[4] Bordbar MH, Hyppänen T. Modeling of radiation heat transfer in a boiler furnace. Adv Stud Theor Phys 2007;1(12):571–84.
[5] Johansson R, Leckner B, Andersson K, Johnsson F. Influence of particle and gas radiation in oxy-fuel combustion. Int J Heat Mass Transfer 2013;65:143–52. http://dx.doi.org/10.1016/j.ijheatmasstransfer.2013.05.073.
[6] Gronarz T, Habermehl M, Kneer R. Modeling of particle radiative properties in coal combustion depending on burnout. Heat Mass Transf 2017;53:1225–35. http://dx.doi.org/10.1007/s00231-016-1896-0.
[7] Gronarz T, Habermehl M, Kneer R. Modeling of particle radiation interaction in solid fuel combustion with artificial neural networks. J Power Technol 2016;96:206–11. http://dx.doi.org/10.1364/AO.35.003270.
[8] Gronarz T, Schulze J, Laemmerhold M, Graeser P, Gorewoda J, Kez V, et al. Quantification of the influence of parameters determining radiaitve heat transfer in an oxy-fuel operated boiler. Fuel Process Technol 2017;157:76–89. http://dx.doi.org/10.1016/j.fuproc.2016.11.012.
[9] Mie G. Beiträge zur Optik trüber Medien, speziell kolloidaler Metallösungen. Ann Phys, Lpz 1908;330(3):377–445. http://dx.doi.org/10.1002/andp.19083300302.
[10] Modest M. Radiative heat transfer. Academic Press; 2013.
[11] Gronarz T, Schnell T, Siewert C, Schneider L, Schröder W, Kneer R. Comparison of scattering behaviour for spherical and non-spherical particles in pulverized coal combustion. Int J Therm Sci 2017;111:116–28. http://dx.doi.org/10.1016/j.ijthermalsci.2016.08.014.
[12] Gronarz T, Höges C, Kez V, Habermehl M, Kneer R. Comparison of scattering behaviour for inhomogeneous particles in pulverized coal combustion. Int J Therm Sci 2019;140:1–7. http://dx.doi.org/10.1016/j.ijthermalsci.2019.02.034.
[13] Koch M, Pielsticker S, Kneer R. Biomass particle-radiation-interaction and the effect of shape and structure simplifications. Fuel 2024;361:130657. http://dx.doi.org/10.1016/j.fuel.2023.130657.
[14] Sarpong E, Smith D, Pokhrel R, Fiddler MN, Bililign S. Refractive indices of biomass burning aerosols obtained from African biomass fuels using RDG approximation. Atmosphere 2020;11(1):62. http://dx.doi.org/10.3390/atmos11010062.
[15] Foster P, Howarth C. Optical constants of carbons and coals in the infrared. Carbon 1968;6(5):719–29. http://dx.doi.org/10.1016/0008-6223(68)90016-X.
[16] Mengüç M, Manickavasagam S, D'Sa D. Determination of radiative properties of pulverized coal particles from experiments. Fuel 1994;73(4):613–25. http://dx.doi.org/10.1016/0016-2361(94)90048-5.
[17] Brewster M, Kunitomo T. The optical constants of coal, char, and limestone. J Heat Mass Transf 1984. http://dx.doi.org/10.1115/1.3246738.
[18] Im K, Ahluwalia R. Radiation properties of coal combustion products. Int J Heat Mass Transfer 1993;36(2):293–302. http://dx.doi.org/10.1016/0017-9310(93)80005-F.
[19] Manickavasagam S, Menguc M. Effective optical properties of pulverized coal particles determined from FT-IR spectrometer experiments. Energy & Fuels 1993;7(6):860–9.
[20] Koch M, Lukas P, Gu Y, Schiemann M, Rohlfs W, Kneer R. Comparison of scattering phase functions of reacting and non-reacting pulverised fuel particles. Fuel 2021;287:119415. http://dx.doi.org/10.1016/j.fuel.2020.119415.
[21] Bohren CF, Huffman DR. Absorption and scattering of light by small particles. John Wiley & Sons; 2008.
[22] Hulst HC, van de Hulst HC. Light scattering by small particles. Courier Corporation; 1981.
[23] Bohren CF. How can a particle absorb more than the light incident on it? Am J Phys 1983;51(4):323–7. http://dx.doi.org/10.1119/1.13262.
[24] Draine BT, Flatau PJ. Discrete-dipole approximation for scattering calculations. Josa a 1994;11(4):1491–9. http://dx.doi.org/10.1364/JOSAA.11.001491.
[25] Mishchenko MI, Travis LD, Mackowski DW. T-matrix computations of light scattering by nonspherical particles: A review. J Quant Spectrosc Radiat Transfer 1996;55(5):535–75. http://dx.doi.org/10.1016/0022-4073(96)00002-7.
[26] Rayleigh L. On the transmission of light through an atmosphere containing small particles in suspension, and on the origin of the blue of the sky. Lond Edinb Dublin Philos Mag J Sci 1899;47(287):375–84. http://dx.doi.org/10.1080/14786449908621276.
[27] Schuster A. An introduction to the theory of optics. E. Arnold; 1904.
[28] Mätzler C. MATLAB functions for mie scattering and absorption, version 2. 2002.
[29] Marzo A, Seah SA, Drinkwater BW, Sahoo DR, Long B, Subramanian S. Holographic acoustic elements for manipulation of levitated objects. Nat Commun 2015;6(1):8661.

[30] Marzo A, Barnes A, Drinkwater BW. TinyLev: A multi-emitter single-axis acoustic levitator. Rev Sci Instrum 2017;88(8). http://dx.doi.org/10.1063/1.4989995.

[31] Groetsch CW, Groetsch C. Inverse problems in the mathematical sciences. vol. 52, Springer; 1993.

[32] Potra FA, Wright SJ. Interior-point methods. J Comput Appl Math 2000;124(1–2):281–302. http://dx.doi.org/10.1016/S0377-0427(00)00433-7.

[33] Böttger J, Eckhard T, Pflieger C, Senneca O, Muhler M, Cerciello F. Green coal substitutes for boilers through hydrothermal carbonization of biomass: pyrolysis and combustion behavior. Fuel 2023;344:128025.